Journal of Alloys and Compounds 509 (2011) 4041–4046

Contents lists available at ScienceDirect

Journal of Alloys and Compounds

journal homepage: www.elsevier.com/locate/jallcom

Microstructure evolution of directionally solidified Ti–45Al–8.5Nb–(W, B, Y) alloys

X.F. Ding, J.P. Lin*, H. Qi, L.Q. Zhang, X.P. Song, G.L. Chen

State Key Laboratory for Advanced Metals and Materials, University of Science and Technology Beijing, Beijing 100083, China

ARTICLE INFO

Article history:
Received 1 December 2010
Received in revised form
29 December 2010
Accepted 4 January 2011
Available online 5 January 2011

Keywords:
Intermetallics
Microstructure
Directional solidification
Crystal growth
Segregation

ABSTRACT

Intermetallic Ti–45Al–8.5Nb–(W, B, Y) alloys were directionally solidified at constant growth rates (V) ranging from 10 to 400 μm/s under the temperature gradient $G = 3.8 \times 10^3$ K/m. Quenching was performed at the end of directional solidification (DS) experiments. Microstructure evolution was investigated by analyzing the microstructures formed at the quenching interfaces and in the DS regions. The primary dendritic arm spacing (λ) decreases with increasing growth rate according to the relationship $\lambda \propto V^{-0.36}$. Both the width of columnar grain (λ_w) and the interlamellar spacing (λ_s) decrease with increasing growth rate according to the relationships $\lambda_w \propto V^{-1.13}$ and $\lambda_s \propto V^{-0.32}$, respectively. Lamellar microstructure initially disappears from the dendrites at the growth rate of 100 μm/s and subsequently from the interdendritic regions when the growth rate is up to 200 μm/s. The B2 particles can precipitate in the interdendritic regions.

© 2011 Elsevier B.V. All rights reserved.

1. Introduction

In recent years, multiphase TiAl-based alloys have been extensively studied as a potential group of materials for high temperature structural applications replacements [1,2]. High Nb containing TiAl alloys have better tensile strength, excellent oxidation resistance and good creep property at elevated temperature compared with conventional TiAl alloys [3–5]. However, improvements in room temperature (RT) properties are necessary before it can be used in load-bearing applications. Directional solidification (DS) is one of the key processing techniques for producing advanced engineering components since it allows a close control of the microstructure, thus of the properties. Both the solidification procedure and the solidification route can be controlled by modifying the parameters during the DS process.

As we know, polysynthetically twinned crystals (PST), achieved by the DS with the seeding technique, exhibit a good balance of tensile strength and ductility when the lamellar orientation is aligned parallel to the tensile axis [6–8]. However, it is still difficult to align the lamellar orientations in peritectic TiAl alloys with the primary β solidification, not to mention in the practice of engineering. The growth morphology, peritectic reaction/transformation and subsequent solid-state transformation are key factors to influence the microstructures of the directionally solidified TiAl alloys, and which greatly increase the difficulty in microstructure control during DS of the high Nb containing TiAl alloys. The tendency of microstructure evolution should be investigated previously in order to control the lamellar microstructure.

This paper presented an experimental investigation on the microstructure evolution of the directionally solidified Ti–45Al–8.5Nb–(W, B, Y) alloys under a lower temperature gradient (G). The effects of growth rate (V) on the growth morphology, the phase transition and the segregation pattern of the directionally solidified alloys were determined. The influences of both peritectic transformation and growth rate on the lamellar microstructures were also studied. These results may help to control the microstructures during the DS of the peritectic TiAl alloys.

2. Experimental procedure

The alloy chosen for this study is Ti–45Al–8.5Nb–0.2W–0.02B–0.02Y (at.%). It was supplied in the form of a cast cylindrical ingot, which was made by the plasma arc melting (PAM). The chemical composition of the ingot was Ti–45.27Al–8.39Nb–(W, B, Y) (at.%), and the oxygen content was less than 640 ppm. The ingot was cut into the cylinder bars with diameter of 6.5 mm and length of 80 mm, and the bars were independently placed into the alumina crucibles, which had been coated by yttria. The DS was performed under 380 Pa high-purity argon by using the Bridgman vertical vacuum furnace. The directionally solidified bars were grown under $G = 3.8 \times 10^3$ K/m and at constant growth rates of 10, 20, 30, 50, 80, 100, 200, and 400 μm/s, respectively. After drawing downward to 40 mm length, quenching was performed immediately.

The directionally solidified bars were sectioned longitudinally, and cut transversely in the DS regions. After polished using standard metallographic techniques, microstructure analyses were studied with the use of field emission scanning electron microscope (FEM) adopting the back-scattered electron (BSE) imaging mode. An optical microscope (OM) was used to characterize the longitudinal macrostructure after etched in a solution of 5 ml HF, 10 ml HNO_3 and 85 ml H_2O.

* Corresponding author. Tel.: +86 10 62332192; fax: +86 10 62333447.
E-mail address: linjunpin@skl.ustb.edu.cn (J.P. Lin).

0925-8388/$ – see front matter © 2011 Elsevier B.V. All rights reserved.
doi:10.1016/j.jallcom.2011.01.014

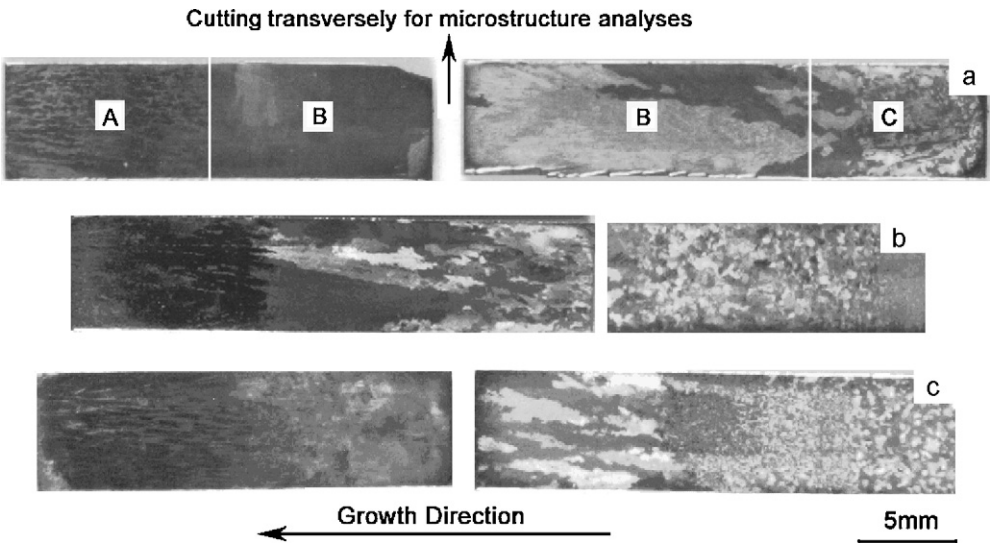

Fig. 1. Macrostructures in longitudinal sections of the DS bars grown at growth rates of (a) 10 μm/s, (b) 20 μm/s and (c) V = 100 μm/s.

The primary dendritic spacing was measured on the distances between the two closest primary arm axes at quenched solid/liquid front, and between the two closest centers of the β-segregation morphologies by examining the BSE microstructures in transversal sections of the directionally solidified bars. The size of columnar grain was determined by the widths of columnar grains in the place where just get into the DS regions in longitudinal macrostructures. The interlamellar spacing was evaluated on the thicknesses of $\alpha_2 + \gamma$ laths of the lamellar microstructures in transversal sections. The statistic analysis of the sizes of Y_2O_3 particles was performed in transversal microstructures of the directionally solidified bars. After measured for hundreds of times, they were independently obtained by calculating the mean value of the measurements at each growth rate.

3. Results and discussion

3.1. Macrostructure

Fig. 1 shows examples of the longitudinal macrostructures observed in quenched bars grown at 10, 20 and 100 μm/s. There are three distinguished sections in the directionally solidified bar performed by the Bridgman DS, which are the quenching region (region A), the DS region with columnar grains (region B), and the non-directional region (region C). Region B is disconnected because a portion of the bar was sectioned transversely for microstructure analysis. As shown in Fig. 2, the number of columnar grains in region B depends on the applied growth rate and the position in the DS bars. It increases with increasing growth rate and with increasing distance from the upper part of the bars. At growth rate of 10 μm/s, some columnar grains eventually combine into one columnar grain after growing for a distance. However, it is an unsteady state, and any fluctuation will possibly induce other grains' crystallization.

3.2. Microstructure

3.2.1. Microstructure at quenched solid/liquid interface

Fig. 2 shows the typical BSE microstructures at quenched solid/liquid interfaces. The growth direction in the figure is from left to right. Few irregular Y_2O_3 particles exhibit white contrast in the microstructures in quenching region. The Y_2O_3 particles were incorporated the melt due to the thermal impaction and convection applied to the yttria coating during the DS process. Even so, the microstructures of the DS alloys can still be predicted because the yttria was hardly reacted with the melting. As shown in Fig. 2, dendritic (Fig. 2(a)–(e)) and dendritic/cellular (Fig. 2(f)) morphologies were found at the solid/liquid fronts. The dendritic length increases with decreasing G/V ratio in the dendrite regime. Primary dendritic arms, as well as secondary dendritic arms, get closer to each other with increasing the growth rate. The phase selection at high velocities should be described by the maximum growth temperature criterion and depend on the velocity only [9], so the primary solidification phase is correspondence to the most stable phase at high growth rate. Secondary dendrite arms are vertical to the primary arms, which can be clearly identified at high growth rate. Four-fold symmetry of dendrites suggests cubic crystal structure of β phase is the primary solidification phase.

The dendritic and dendritic/cellular growth morphologies were studied extensively [10–12]. The primary dendritie tip radius decreases with increase of the growth rate. Some dendrites grow with an inclined angle of about 30° to the growth direction possibly due to an underlying cubic symmetry (Fig. 2(c)) [13]. The growths of higher-order branches are restrained by coarsen of secondary ones when the growth rate is increased. At the stage of dendrite/cell transition, the dendrite grows unstably, and exhibits with shorter length and inhomogeneous breadth shape (Fig. 2(f)). The measured primary dendritic spacing (λ) decreases proportionally with increasing growth rate according to the following relationship [14]:

$$\lambda = M \cdot V^n \quad (1)$$

where M is a material constant and n is the exponent of crystallization rate. Regression analysis of experimental data yields an equation in the form:

$$\lambda = 1.1 \times 10^3 \cdot V^{-0.36} \quad (2)$$

The regression coefficient of the fit is $R^2 = 0.96$ and the result is shown in Fig. 3. It agrees to Hunt's primary spacing model in which it indicates $\lambda \propto V^{-1/4} \sim V^{-1/2}$ [15].

3.2.2. Microstructure in the DS region

Fig. 4 presents the typical microstructures in the DS regions of the directionally solidified bars at a series of growth rates raging from 10 to 400 μm/s [16]. The growth directions in the longitudinal sections are all from left to right. A wide variety of microstructures can be observed from the BSE images of the bars. Al-segregation in dark-grey contrast and β-formers segregation (β-segregation) in bright-grey contrast are generated in the interdendritic and dendritic regions, respectively. The fully lamellar (FL) microstructures ($\alpha_2 + \gamma$) with different segregation patterns are observed when the growth rate is less than 80 μm/s, as shown in Fig. 4A–E. At the growth rate of 100 μm/s (Fig. 4F), the lamellar microstructure ini-

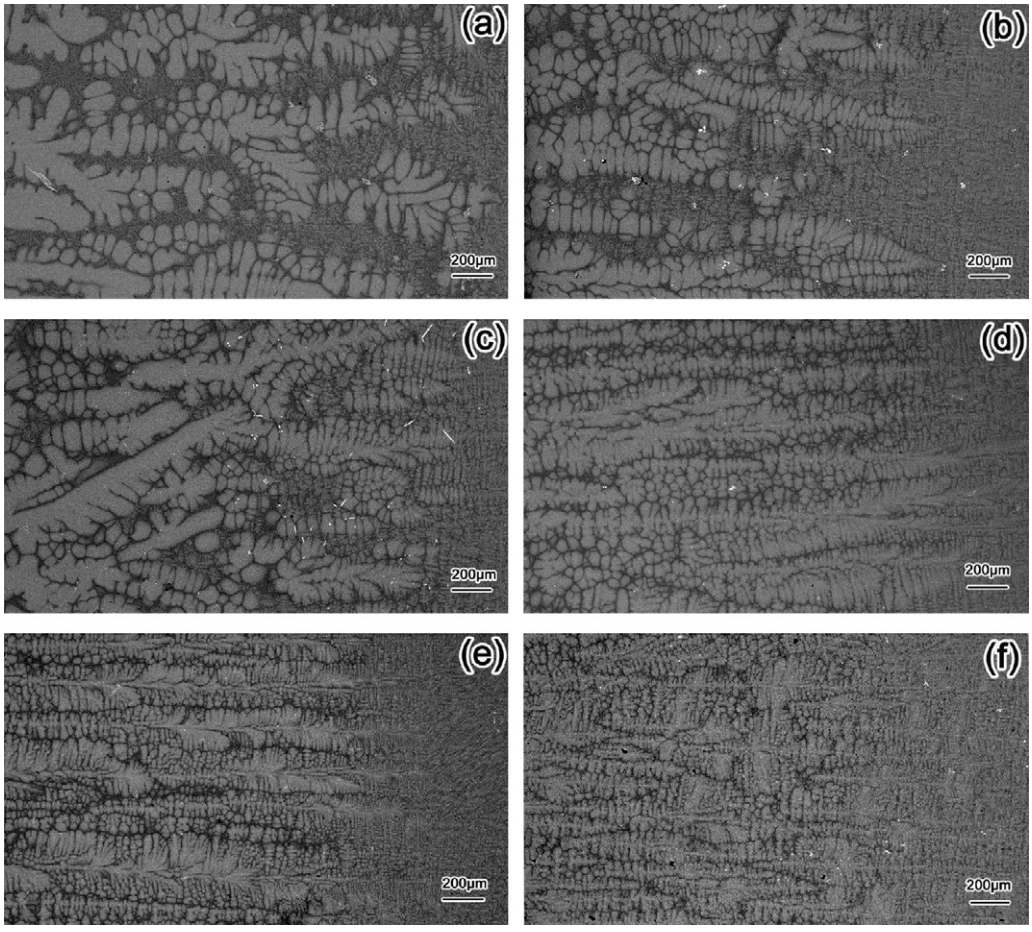

Fig. 2. BSE microstructures at the quenched solid/liquid interfaces of the DS bars at growth rates of (a) 10 μm/s, (b) 20 μm/s, (c) 30 μm/s, (d) 100 μm/s, (e) 200 μm/s and (f) 400 μm/s.

tially disappears from the arm of dendrite, and subsequently from the interdendritic region when the growth rate is greater than 200 μm/s (Fig. 4G). Apart from the Y_2O_3 particles, a small volume fraction of elongated B2 particles is found in the interdendritic regions.

The dendritic structure with a peritectic phase enveloped primary dendrites with signs of partial solid-state transformation is usually produced at lower G/V ratios [17]. During the peritectic solidification in primary β TiAl alloys, the β dendrite is partially transformed peritectically into the α phase, and then the residual β is directly transformed into α grains by the solid-state transformation $\beta \rightarrow \alpha$. The β-formers, such as Ti and Nb, are segregated into the dendrites and Al is rejected into the interdendrites. In the dendrite regime, Al–solute rejection of the tips increases with growth rate, which leads to the increasing undercooling [18]. Peritectic phase α envelops primary phase β by the peritectic reaction at the positions in the growth direction behind the β tips. Peritectic transformation occurs when the properitectic β is isolated by peritectic α. The peritectic α can be thickened by dissolving the properitectic β phase and the direct precipitation of α phase toward the liquid. However, the peritectic transformation is difficult to be completed due to the low diffusion coefficient in the solid phase. The high-temperature α phase can be produced by the $\beta \rightarrow \alpha$ solid-state transformation from the residual β phase as well as the peritectic reaction and transformation.

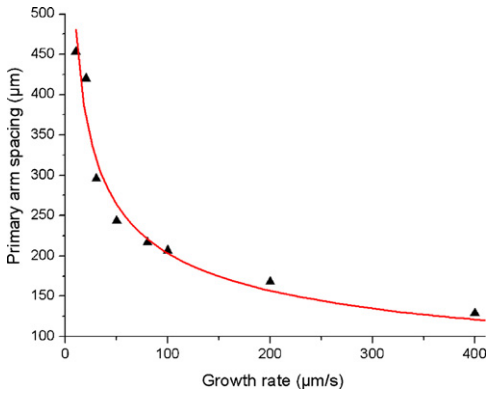

Fig. 3. Dependence of the primary dendritic arm spacing on the growth rate.

The pattern of Al-segregations depends on the morphology of properitectic β dendrites and the formation of peritectic α during DS process. The upright dendrites induce to an aligned pattern of interdendritic Al-segregation. At lower growth rate, the direct precipitation of peritectic α can move the liquid/solid interface forward toward the interdendrite, and eventually make the pattern with a regular column (Fig. 4A and B). When the growth rate is increased, some primary dendrites angled to the growth direction result in the irregular Al-segregation patterns (Fig. 4C and D). Fig. 4E shows the Al-segregation pattern mainly caused by the growth of equiaxed dendrites and the subsequent peritectic transformation. At higher growth rates, local enrichment of interdendritic liquid by Al and less solution diffusion lead to formation of γ phase (Fig. 4G and H). Massive or $\alpha \rightarrow \alpha_2$ transformation is supposed to occur

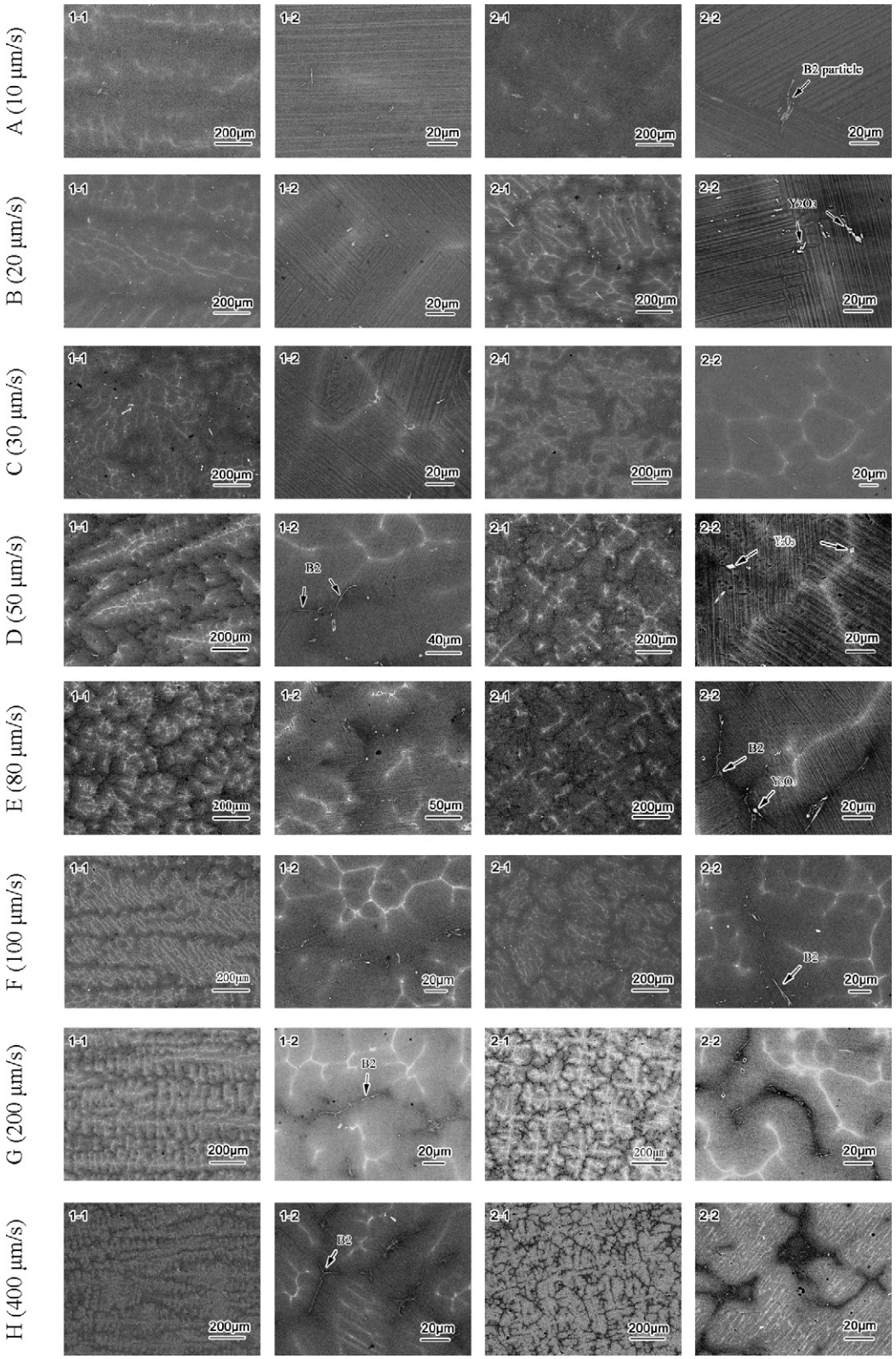

Fig. 4. Typical BSE microstructures in the DS regions of the directionally solidified bars at the growth rates ranging from 10 to 400 μm/s showing the microstructures in: longitudinal sections with low-magnification (1-1) [16], longitudinal sections with high-magnification (1-2), transversal sections with low-magnification (2-1) and transversal sections with high-magnification (2-2).

in dendritic regions (Fig. 4F–H). High containing of β-formers in Al–lean dendrites can lead to the massive transformation and even $\alpha \rightarrow \alpha_2$ transformation at a normal cooling rate [19,20]. Therefore, deviating from the equilibrium solidification, meta-stable α, even γ can also grow from liquid [18,21], which may lead to the transition sequences as follows:

$$\text{Liq.} \rightarrow \text{Liq.} + \beta \quad (\text{dendritic}) + \alpha \quad (\text{interdenditic}) \rightarrow \text{lamellae} \quad (\alpha_2 + \gamma) + \text{B2} \tag{3}$$

$$\text{Liq.} \rightarrow \text{Liq.} + \beta \quad (\text{dendritic}) + \gamma \quad (\text{interdendritic}) \rightarrow \alpha_2 + \gamma + \text{B2} \tag{4}$$

Table 1
Statistics on the morphology of properitectic β, types of microstructure and major transformation, width of columnar grain and interlamellar spacing at different growth rates (FL: fully lamellar, PL: partially lamellar and UL: un-lamellar).

Growth rate (μm/s)	Morphology of properitectic β	Type of microstructure	Major transformation	Width of columnar grain (mm)	Interlamellar spacing (μm)
10	Upright dendrite	FL	Peritectic	3.8	3.2
20	Upright dendrite	FL	β → α	2.1	2.8
30	Inclined dendrite	FL	β → α	0.85	2.2
50	Inclined dendrite	FL	Peritectic	0.49	1.9
80	Upright dendrite	FL	Peritectic	0.44	1.7
100	Upright dendrite	PL	β → α	0.28	–
200	Upright dendrite	UL	Peritectic	–	–
400	Upright dendrite/cell	UL	β → α	–	–

As indicated by Chen et al. [22], the solid-state transformation of β → α can result in the nucleations of several α grains in a single β grain and the formations of β-segregations, even B2 phases at the interfaces between the β and α grains. After the peritectic transformation, a small volume fraction of residual β phase is responsible for the segregation of β-formers centralized in the cores of dendritic arms. So the β-segregation pattern within the primary dendrites in transversal section (series of 2-1 in Fig. 4) can be used to recognize the high-temperature α mainly formed by the peritectic L + β → α or the solid-state β → α transformation. If the pattern of β-segregation displays four-fold symmetry, peritectic transformation should be more completed, thus more advantageous in subsequent transformation, and if the pattern shows a decentralized and reticular formation within the dendrites, it should cause by the solid-state transformation of β → α. Since the diffusion depends on the distance and the cooling rate, the type of transformation is significant influenced by the dendritic morphology of properitectic β as well as the growth rate. An overview of the morphology of properitectic β, the types of microstructure and major transformation at different growth rates are summarized in Table 1.

The tensile properties of directionally solidified TiAl alloys were reported to be better when the lamellar boundaries are aligned parallel to the growth direction [23]. However, the lamellar orientation is observed to be changed mostly nearby the boundaries of dendrites or around the β-segregations (Fig. 4B–E). The lamellar structure of TiAl-based alloys consists of lamellae of the γ and α_2 (ordered α) phases with the orientation relationship $(1\,1\,1)_\gamma//(0\,0\,0\,1)_{\alpha_2}$ and the transformation of β → α keeps the relationship $[0\,0\,0\,\bar{1}]_\alpha//[1\,1\,0]_\beta$ [23]. Accordingly, the lamellar orientation is determined by the growth of the parent α-phase, and the β → α solid-state transformation is obviously harmful to align the high-temperature α, thus the lamellar orientation. Twelve α variants with different orientations can be generated by the β → α solid-state transformation in dendritic region [24]. In comparison, the peritectic transformation L + β → α can produce the larger α grains, thus a larger area of lamellar microstructures with aligned lamellar orientation. Only one lamellar grain in the upper part of the bar is most likely caused by the closely completed peritectic transformation during the DS at growth rate of 10 μm/s (Fig. 4A).

Both of the width of columnar grain and the interlamellar spacing are also closely related to the mechanical properties of the directionally solidified alloys. Table 1 also presents the mean values of them at different growth rates. Variations of both the width of columnar grain and the interlamellar spacing with growth rate are summarized in Fig. 5. The calculated mean values of both the width of columnar grain (λ_w) and the interlamellar spacing (λ_s) decrease proportionally with increasing growth rate according to the following relationship:

$$\lambda_{w/s} = K \cdot V^a \quad (5)$$

where K is a material constant and a is the rate exponent. Using regression analysis, the dependences of the grain's width and the interlamellar spacing on the growth rate can be expressed in the forms of

$$\lambda_w = 52.1 \cdot V^{-1.13} \quad (6)$$

and

$$\lambda_s = 6.79 \cdot V^{-0.32} \quad (7)$$

The regression coefficients of these fits are $R_w^2 = 0.98$ and $R_s^2 = 0.97$, respectively.

Due to the high stability to the high activity of titanium melt, CaO and Y_2O_3 crucibles should be the prior ones to produce the directionally solidified TiAl-based castings, however, the easy deliquescence of CaO crucibles and the high hot brittleness of Y_2O_3 ones limit their wide use [25]. In our study, the yttria-coated Al_2O_3 crucibles were used in the DS process. Long-term interactions between the TiAl melt and the coated alumina crucibles during DS can result in contamination of melt by yttria inclusions. A highly increased oxygen level from 640 to 2600 wt. ppm was detected after the DS was performed at the growth rate of 10 μm/s. The sizes of the yttria particles increase with the decreasing growth rate and the increasing time in which the melting contacts with the coated crucible. Fig. 6 shows the variation of the size of Y_2O_3 particle (S) with the growth rate V. The sizes of Y_2O_3 particles decrease dramatically with decreasing growth rate. Their sizes are less than 20 μm when V is greater than 30 μm/s. The dependence of the size of Y_2O_3 particle on the growth rate is also presented in the figure.

Additionally, a small volume fraction of elongated B2 particles was observed in interdendritic region (Fig. 4). As it indicated by Lapin et al. [26], B2 particles can be formed in the interdendritic region in the directionally solidified TiAl alloys with addition of β-stabilizer, such as Nb. A very small volume-fractioned β-stabilizers may be dissolved in the interdendritic region, and then centralized and combined into B2 particles during cooling. The interdendritic

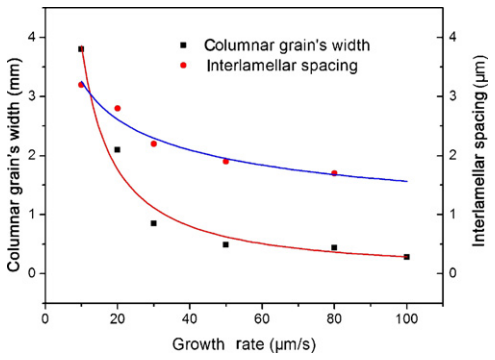

Fig. 5. Variations of both the columnar grain's width and the interlamellar spacing with the growth rate.

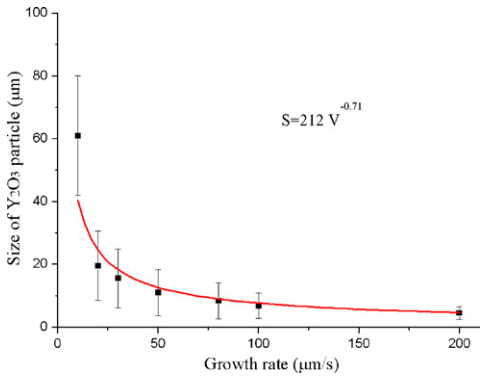

Fig. 6. Variation of the size of Y_2O_3 particle (S) with the growth rates (V).

B2 particles disrupt the continuity of the lamellar microstructures, and coarse γ phases are formed adjacently to the B2 phases [27]. Increasing growth rate will result in increasing of the volume fraction of the B2 particles [21], eventually reduce the mechanical properties of the directionally solidified alloys.

4. Conclusions

Microstructure evolution of the directionally solidified Ti–45Al–8.5Nb–(W, B, Y) alloys was investigated at the growth rates (V) ranging from 10 to 400 μm/s under the temperature gradient $G = 3.8 \times 10^3$ K/m. The following conclusions can be drawn from the present results:

1. The dendritic and dendritic/cellular structures with peritectic α phase enveloped primary β dendrites are developed at the growth rate less than 100 μm/s. The primary β dendritic arm spacing λ decreases with increasing growth rate according to the relationship of $\lambda \propto V^{-0.36}$.
2. Different solidification procedures have been experienced in the dendritic and interdendritic regions with increase of the growth rate. FL microstructures are achieved when the growth rate is less than 80 μm/s. Lamellar microstructure initially disappears from the arm of dendrite at the growth rate of 100 μm/s and subsequently from the interdendritic region when the growth rate is increased to 200 μm/s. The α_2 and γ phases can be produced in the dendritic and interdendritic regions, respectively.
3. The peritectic transformation $L + \beta \rightarrow \alpha$ or the solid-state transformation $\beta \rightarrow \alpha$, which has been experienced in dendritic region, can be recognized by the pattern of β-segregation within the primary dendrite. The width of columnar grain λ_w and the interlamellar spacing λ_s increase with decreasing growth rate according to the relationships $\lambda_w \propto V^{-1.13}$ and $\lambda_s \propto V^{-0.32}$, respectively. B2 particles are formed in the interdendritic regions.

Acknowledgements

This research was financially supported by the National Basic Research Program of China (973 Program) under contract No. 2011CB605500 and the National Natural Science Foundation of China under grant No. 50871127 project.

References

[1] E.A. Loria, Intermetallics 8 (2000) 1339–1345.
[2] M. Yamaguchi, H. Inui, K. Ito, Acta Mater. 48 (2000) 307–322.
[3] G.L. Chen, W.J. Zhang, Z.C. Liu, S.J. Li, Y.W. Kim, in: Y.W. Kim, D.M. Dimiduk, M.H. Loretto (Eds.), Gamma Titanium Aluminides, TMS, Warrendale, PA, 1999, pp. 371–380.
[4] X.J. Xu, J.P. Lin, Y.L. Wang, J.F. Gao, Z. Lin, G.L. Chen, J. Alloys Compd. 414 (2006) 131–136.
[5] J.P. Lin, X.J. Xu, Y.L. Wang, S.F. He, Y. Zhang, X.P. Song, G.L. Chen, Intermetallics 15 (2007) 668–674.
[6] S. Yokoshima, M. Yamaguchi, Acta Mater. 44 (1996) 873–883.
[7] M.H. Oh, H. Inui, M. Misaki, M. Yamaguchi, Acta Metall. Mater. 41 (1993) 1939–1949.
[8] R. Lebensohn, H. Uhlenhut, C. Hartig, H. meckin, Acta Mater. 46 (1998) 4701–4709.
[9] O. Hunziker, M. Vandyoussefi, W. Kurz, Acta Mater. 46 (1998) 6325–6336.
[10] J.S. Langer, H. Muller-Krumbhaar, Acta Metall. 26 (1978) 1681–1719.
[11] W. Kurz, D.J. Fisher, Acta Metall. 29 (1981) 11–20.
[12] S.Z. Lu, J.D. Hunt, J. Cryst. Growth 123 (1992) 17–34.
[13] T. Haxhimali, A. Karma, F. gonzales, M. rappaz, Nat. Mater. 660 (2006) 660–664.
[14] T.S. Lo, S. Dobler, M. Plapp, A. Karma, W. Kurz, Acta Mater. 51 (2003) 599–611.
[15] J.D. Hunt, S. Lu, Metall. Mater. Trans. A 27 (1996) 611–623.
[16] X.F. Ding, J.P. Lin, L.Q. Zhang, X.P. Song, G.L. Chen, Mater. Des. 32 (2011) 395–400.
[17] S. Dobler, T.S. Lo, M. Plapp, A. Karma, W. Kurz, Acta Mater. 52 (2004) 2795–2808.
[18] T. Umedaa, T. Okanea, W. Kurz, Acta Mater. 44 (1996) 4209–4216.
[19] A. Huang, D. Hu, X. Wu, M.H. Loretto, Intermetallics 15 (2007) 1147–1155.
[20] Q.F. Xia, J.N. Wang, J. Yang, Y. Wang, Intermetallics 9 (2001) 361–367.
[21] X.F. Ding, J.P. Lin, L.Q. Zhang, H.L. Wang, G.J. Hao, G.L. Chen, J. Alloys Compd. 506 (2010) 115–119.
[22] G.L. Chen, X.J. Xu, Z.K. Teng, Y.L. Wang, J.P. Lin, Intermetallics 15 (2007) 625–631.
[23] M. Yamaguchi, D.R. Johnson, H.N. Lee, H. Inui, Intermetallics 8 (2000) 511–517.
[24] W.G. Burgers, Physica 1 (1934) 561–586.
[25] D. Liu, X. Li, Y. Su, J. Guo, H. Fu, Intermetallics 19 (2011) 175–181.
[26] J. Lapin, L. Ondr, M. Nazmy, Intermetallics 10 (2002) 1019–1031.
[27] H.N. Lee, D.R. Johnson, H. Inui, M.H. Oh, D.M. Wee, M. Yamaguchi, Acta Mater. 48 (2000) 3221–3233.